

Equilibrium wall-modeled LES of shock-induced aerodynamic heating in hypersonic boundary layers

By L. Fu, M. Karp, S. T. Bose,
P. Moin AND J. Urzay

1. Motivation and objectives

Fuselages and airbreathing propulsion systems of hypersonic vehicles are often subject to large thermomechanical loads related to shock-induced phenomena (Urzay 2018). The high airflow velocities associated with hypersonic flight complicate the description by introducing a number of intricate gasdynamic effects (Candler 2019). A relevant problem of interest for hypersonic aerodynamics is the interaction of incident shock waves with hypersonic boundary layers (Leyva 2017).

The subject of this study is the interaction of incident oblique shocks with hypersonic transitional boundary layers overriding a cold isothermal flat plate. In particular, equilibrium wall-modeled large-eddy simulations (WMLES) are employed with the intent of predicting the physical processes responsible for the intense overheating downstream of the shock-impingement region, where the boundary layer suddenly transitions to turbulence, as depicted in Figure 1. The WMLES predictions are compared against direct numerical simulations (DNS).

In contrast to recent work that has focused on relatively shallow shock-incidence angles (Sandham *et al.* 2014; Yang *et al.* 2017; Mettu & Subbareddy 2018), for which inlet disturbances are necessary for the boundary layer to transition, the present work focuses on higher angles, for which no inlet disturbances are required since the adverse pressure gradient generated by the shock wave is sufficiently strong to be the main factor for boundary-layer transition, as suggested also in recent stability studies by Hildebrand *et al.* (2018). High shock-incidence angles lead to large and localized wall-heat fluxes immediately downstream of the shock-wave impingement region, which challenges all wall models designed to date. It is anticipated from the results presented below that the equilibrium wall model underperforms quantitatively in the critical interaction region, thereby calling for additional research and wall-model developments in this area.

The remainder of this report is organized as follows. In Section 2, the computational setup is described. Comparisons between WMLES and DNS are given in Section 3. Concluding remarks and open questions are provided in Section 4. Lastly, an Appendix is included with a verification exercise for the laminar portion of the boundary layer.

2. Computational setup

The formulation of the problem is described in Yang *et al.* (2017) and the reader is referred to that paper for details, including the equilibrium wall model for compressible boundary layers utilized here. In short, the conservation equations correspond to mass, momentum, and total energy. Filtered versions of these equations are employed for LES

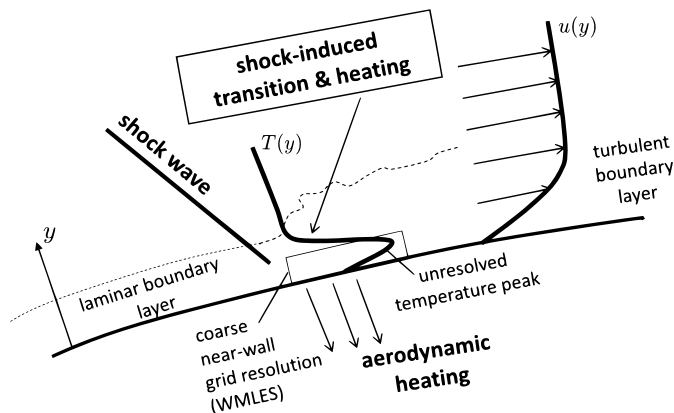


FIGURE 1. Schematics of the model problem.

cases, with the subgrid-scale (SGS) tensor and SGS energy flux being modeled using the constant-coefficient Vreman model (Vreman 2004), with model constant 0.07, along with a constant turbulent Prandtl number $Pr_t = 0.90$. The conservation equations are supplemented with the Sutherland's law for the dynamic viscosity under a constant molecular Prandtl number $Pr = 0.72$ (with Sutherland's model constants satisfying $T_{\text{ref}} = T_\infty$ and $S/T_\infty = 1.69$), the ideal-gas equation of state, and the assumption of calorically-perfect gas with $\gamma = 1.4$. The latter is justified by the low temperatures that prevail in the free stream. In particular, the geometry and operating conditions are inspired by the low-enthalpy experiments described in Schülein (2014), Sandham *et al.* (2014), and Willems *et al.* (2015). Specifically, air at Mach $Ma_\infty = 6.0$ flows over an isothermal flat plate held at temperature $T_w = 4.5T_\infty$, as schematically shown in Figure 2. In these conditions, where T_w is smaller than the free-stream stagnation temperature $T_{0,\infty}$ (i.e., $T_w/T_{0,\infty} = 0.55$), the plate behaves as a cold one that receives heat from the flow as a result of the non-monotonicity of the profile of static temperature in the wall-normal direction, as depicted in Figure 1. This profile is challenging to resolve with WMLES-like coarse grid resolution near the wall. A wedge held above the plate is responsible for generating the shock wave that impinges on the boundary layer. In this work, three wedge angles $\alpha = 6^\circ$, 7° , and 8° are studied, while keeping all other parameters constant. However, the wedge is not included in the computational domain. Instead, the emanating shock is imposed by appropriate boundary conditions, as described below.

The coordinate system $\{x, y, z\}$ used for the analysis is shown in Figure 2, with $x = 0$ corresponding to the leading-edge of the plate. The inlet of the computational domain is located at a distance $x_o/\delta_o^* = 46.1$ downstream of the leading edge, where the Reynolds number is $Re_{\delta_o^*} = 6830$ based on the inlet displacement thickness δ_o^* . Correspondingly, the similarity solution for compressible laminar boundary layers is imposed at the inlet. In addition, periodic boundary conditions are used in the spanwise direction, while a characteristic non-reflecting boundary condition is applied at the outlet with reference pressure equal to the free-stream pressure. For a given wedge angle α , the shock is made to emanate from the top boundary of the domain at a streamwise position x_s such that the point of inviscid intersection between the shock and the plate is located at a streamwise distance x_{imp} from the leading edge of the plate such that $(x_{\text{imp}} - x_o)/\delta_o^* = 150$ in all cases, or equivalently, at a Reynolds number $Re_{x,\text{imp}} = 1.34 \cdot 10^6$ based on the streamwise distance x measured from the leading edge of the plate (see Figure 2). For $x > x_s$, an

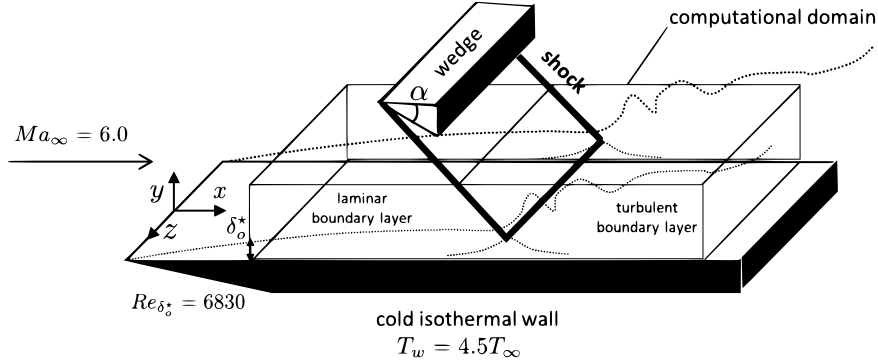


FIGURE 2. Schematics of the computational setup.

oblique flow entering the domain is prescribed at the top boundary using the Rankine-Hugoniot jump conditions for pressure, density and velocities at the corresponding shock strength determined by the wedge angle α , while the discretized fluxes at the boundary cell face are obtained by solving a Riemann problem with an HLLC solver. For $x < x_s$, the similarity solution, including its vertical displacement velocity, is imposed at the top boundary. The simulations were initialized using the similarity solution for the laminar compressible boundary layer in the absence of an incident shock, and were evolved for 26 (in DNS) and 113 (in WMLES) flow-through times before the period of collection of time-averaged statistics began. The latter lasted for 36 (in DNS) and 48 (in WMLES) flow-through times during which cumulative statistics were calculated based on an on-the-fly analysis of the solution at every time step.

The second-order accurate, compressible, finite-volume code CharLES (Brès *et al.* 2018) is employed for the simulations. The numerical method consists of an approximately entropy-preserving scheme that curtails the amount of numerical dissipation deployed in the flow. The dimensions of the computational domain are $300\delta_o^* \times 25\delta_o^* \times 45\delta_o^*$ in the streamwise, wall-normal, and spanwise directions, respectively. All grids are Cartesian, with vertical stretching used only in the DNS cases. The grid sizes are $3000 \times 300 \times 400$ (360M cells) for DNS and $512 \times 64 \times 144$ (4.7M cells) for WMLES. The near-wall resolution in viscous units $\Delta x^+ \times \Delta y^+ \times \Delta z^+$, based on the outlet state of the boundary layer, is $4.4 \times 1.4 \times 4.9$ (for DNS at $\alpha = 6^\circ$), $22.7 \times 15.2 \times 12.1$ (for WMLES at $\alpha = 6^\circ$), $6.1 \times 1.9 \times 6.9$ (for DNS at $\alpha = 7^\circ$), $26.7 \times 17.8 \times 14.2$ (for WMLES at $\alpha = 7^\circ$), $6.7 \times 2.1 \times 7.6$ (for DNS at $\alpha = 8^\circ$), and $30.6 \times 20.4 \times 16.3$ (for WMLES at $\alpha = 8^\circ$). In all WMLES cases, the spanwise-averaged boundary layer was resolved by 4 points across at the inlet boundary (i.e., see Appendix), by 13 points across at the outlet, and by 11 points across at the streamwise location of maximum wall heat flux, or equivalently, the maximum Stanton number St , which is defined below in Section 3.

Non-slip and isothermal boundary conditions are employed at the wall for DNS cases. In WMLES, the equilibrium wall model described in Yang *et al.* (2017) [see also Kawai & Larsson (2012)] is utilized within a wall-modeled layer that has a thickness equivalent to 3 cells of the computational grid. Briefly, the equilibrium wall model consists of localized, RANS-like, steady one-dimensional versions of the wall-parallel momentum equation and the total energy equation, with eddy-viscosity closures for the turbulent transport of momentum and energy, the latter relying on the assumption of constant turbulent Prandtl number $Pr_t = 0.90$ equal to the one used for the bulk flow. The equations of the wall

model are subject to non-slip and isothermal boundary conditions at the wall, and to the instantaneous filtered values of the wall-parallel velocity, temperature, and pressure at the matching location. Since the model does not incorporate streamwise variations, upstream propagation of elliptic effects, for instance due to adverse pressure gradients along subsonic regions, can only occur through the boundary conditions applied at the matching location. The outputs of the model are the local values of the wall shear stress and wall heat flux, which are employed as boundary conditions for the LES conservation equations of the bulk flow.

In these simulations, the equilibrium wall model is applied everywhere along the surface of the plate, including the laminar portion of the boundary layer. It should however be noted that the scenarios sought for transition in this study are not the classical ones in which unstable eigenmodes grow relatively slowly along the boundary layer, eventually producing transition far downstream of the leading edge in a way that is rather well understood, at least for calorically perfect gases flowing over smooth flat surfaces. Instead, transition in the present study occurs suddenly downstream of the shock without any other external disturbances being required. As a result, in the present study there are lesser consequences derived from the fact that neither the coarse grid resolution nor the equilibrium wall model can appropriately support the growth of eigenmodes along the lengthy laminar portion of the boundary layer upstream of the shock. As shown in Figure 8(c,d) in the Appendix, the WMLES cases perform unexpectedly well in predicting the similarity solution upstream of the shock. Nonetheless, this is not to say that WMLES should be used as best practice along laminar portions of the boundary layer, particularly right downstream of the shock in the transitional zone where its utilization may artificially prompt transition, as shown below, and where other alternatives based on transition sensors or parabolized stability equations may perhaps be more appropriate.

3. Results

The following results are focused on comparisons between DNS and WMLES using the skin friction coefficient C_f and the Stanton number St as main figures of merit. The skin friction is defined as $C_f = 2\langle\tau_w\rangle/(\rho_\infty U_\infty^2)$, where U_∞ and ρ_∞ are the free-stream pre-shock values of the velocity and density, respectively, and the angular brackets denote double averaging in time and in the spanwise direction. In this formulation, $\tau_w = \mu_w(\partial u/\partial y)_w$ is the wall shear stress, where u is the streamwise velocity and μ_w is the dynamic viscosity evaluated at the wall temperature. Similarly, the Stanton number is defined as $St = \langle q_w \rangle / [\rho_\infty U_\infty c_p (T_{aw} - T_w)]$, where $q_w = k_w(\partial T/\partial y)_w$ is the wall heat flux, T is the temperature, k_w is the thermal conductivity evaluated at the wall temperature, c_p is the constant-pressure specific heat of the gas, and $T_{aw} = T_\infty[1 + r(\gamma - 1)Ma_\infty^2/2]$ is the adiabatic wall temperature with an approximate recovery factor $r = Pr^{1/2}$.

The distributions of C_f and St as a function of the streamwise Reynolds number Re_x are provided in Figure 3 for the three different wedge angles tested here. In interpreting these results, it is first important to note that the van-Driest's turbulent correlation is based here on pre-shock free-stream conditions, and therefore the post-shock turbulent boundary layers should not be expected to follow it, not even farther downstream. More critical than this necessary mismatch is the fact that the equilibrium wall model is unable to predict the DNS results of C_f and St in any of the three cases for reasons discussed in what follows.

For $\alpha = 6^\circ$, the moderate increases in C_f and St predicted by the DNS results in

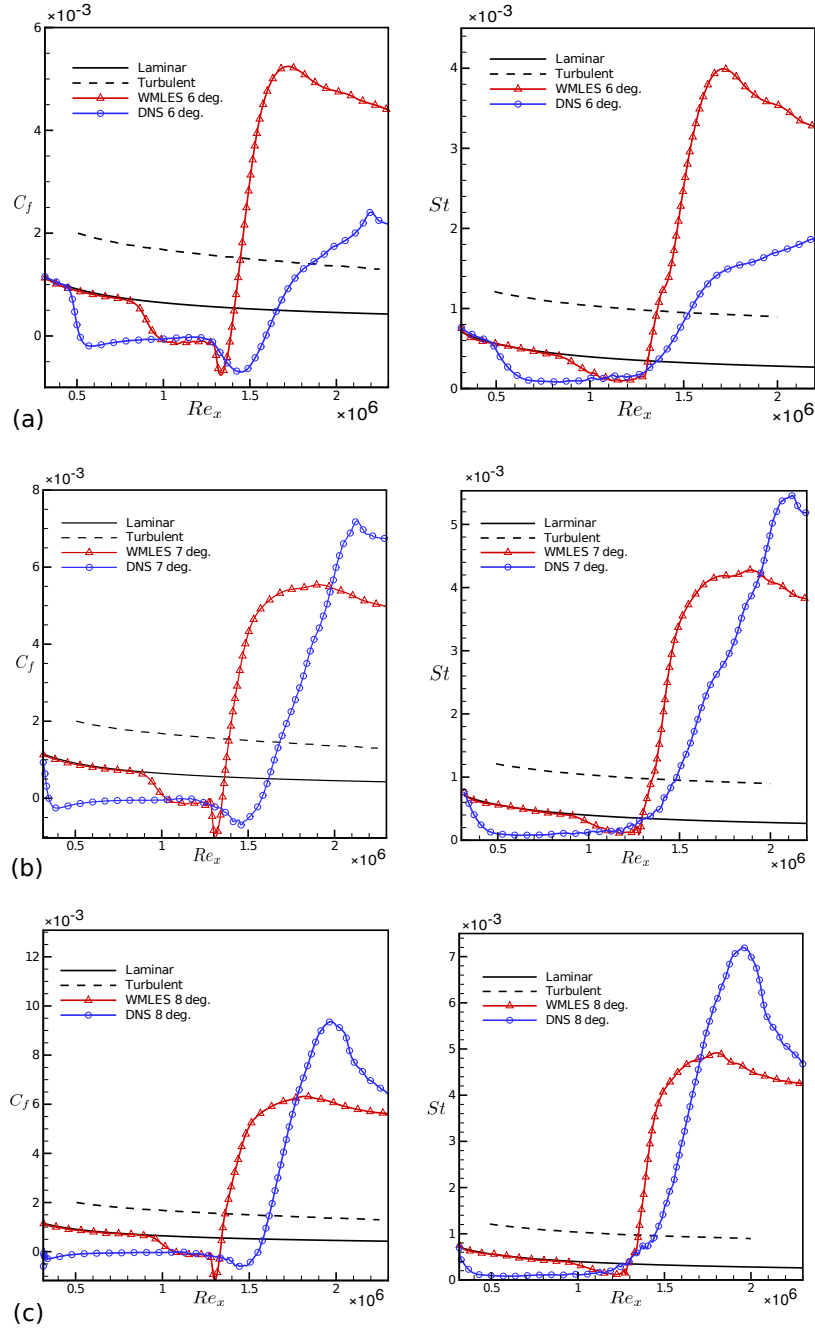


FIGURE 3. Skin friction coefficient (left) and Stanton number (right) for (a) $\alpha = 6^\circ$, (b) 7° , and (c) 8° .

Figure 3(a) upon shock impingement, which are mainly produced by the variation of the free-stream aerothermodynamic state through the shock, suggest that the boundary layer has not fully transitioned into turbulence in the post-shock region. It is already known

that shocks at low incidence angles do not trigger transition without inlet disturbances (Hildebrand *et al.* 2018). Note however, that the negative values of C_f in Figure 3(a) indicate that the shock has produced a separation bubble. The instantaneous density contours provided in the top panel of Figure 4 ratify that the post-shock boundary layer has not transitioned. Dynamic visualizations of the same contours show long-wavelength unsteady oscillations in the post-shock boundary layer whose origins are unclear at the time of writing this report, but could be possibly related to low-frequency breathing motion of the separation bubble. More interestingly, and in contrast to the DNS results, the distributions of C_f and St in the WMLES results in Figure 3(a) are indicative of transition despite the low incidence angle. This is an important shortfall of the WMLES that can also be visualized in the instantaneous density contours in the bottom panel in Figure 4. There, transition is observed to occur promptly downstream of the shock-impingement region for reasons that are most likely related to the inadequacy of employing the wall model everywhere along the surface of the plate, particularly in the interaction region, and most severely in regimes where the shock is not sufficiently strong to cause transition by itself and the coarse WMLES grid is unable to support neither the wavelength of the resulting post-shock instabilities nor their growth over long distances.

The aforementioned discrepancy between DNS and WMLES regarding the existence of transition vanishes in the other two cases $\alpha = 7^\circ$ and 8° . In these cases, the DNS results indicate the occurrence of boundary-layer transition shortly downstream of the shock-impingement region, as expressed by the sharp increases in C_f and St shown in Figure 3(b,c). The WMLES results also predict shock-induced transition, although the transition location is incorrectly shifted upstream in a manner that is reminiscent of the erroneous WMLES prediction in the low-angle case $\alpha = 6^\circ$ described above. Furthermore, the WMLES significantly underpredicts the peak values of C_f and St by up to 30% in the most adverse case $\alpha = 8^\circ$, when the post-shock rise in those quantities in DNS is the largest. In connection with such underprediction is that the flow structures ensuing from the interaction with the shock in DNS are quite different from those predicted by WMLES, as observed in Figures 5 and 6. In particular, the wide transitional streaks predicted by DNS, which carry large values of u' (and corresponding large values of T' as would be qualitatively suggested by the Morkovin's hypothesis), are replaced in LES by narrower and less intense streaks that promptly lead to turbulence. Note that the maximum aerodynamic heating rate in DNS is achieved in this thermally critical zone where the wide streaks develop and where the correspondingly strong longitudinal flow decelerations lead to transformation of kinetic energy into thermal energy, thereby creating hot elongated spots on the wall surface, as seen in the top panel in Figure 6. The causes underlying the absence of these structures in WMLES cases is subject of current investigations as a worthy continuation of this work.

In all cases, WMLES also underpredicts the size of the separation bubble engendered by the interaction of the shock wave with the boundary layer, as observed by the resulting limited extent of the negative portion of the WMLES profiles of C_f in Figure 3, and by the bubble sizes that can be qualitatively inferred from the density contours in Figure 4. The resulting long zone of flow reversal upstream of the shock proves to be difficult to capture even in DNS, as suggested by the profiles of C_f in Figure 3(b,c), which appear to be constrained on the left by the inflow boundary. As commented above, the equilibrium wall model cannot anticipate the presence of a downstream recirculation region or any other elliptic effect, including the propagation of pressure waves along the subsonic region below the sonic line close to the wall, unless information affected by

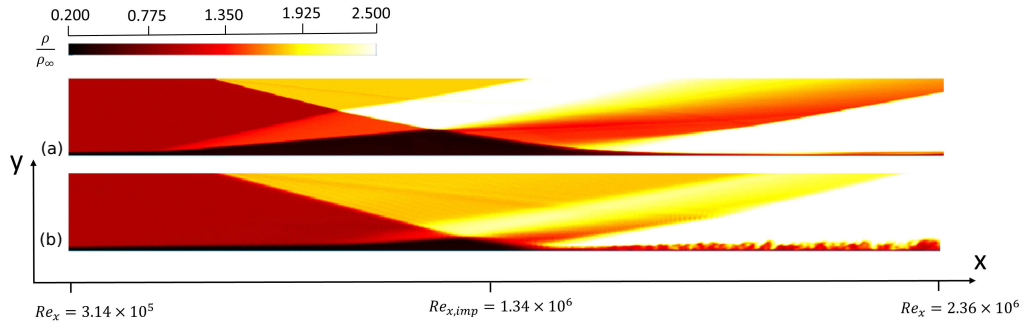


FIGURE 4. Instantaneous density contours for $\alpha = 6^\circ$ on a cross-sectional streamwise-parallel plane located at $z/\delta_o^* = 22.5$ in DNS (top) and WMLES (bottom).

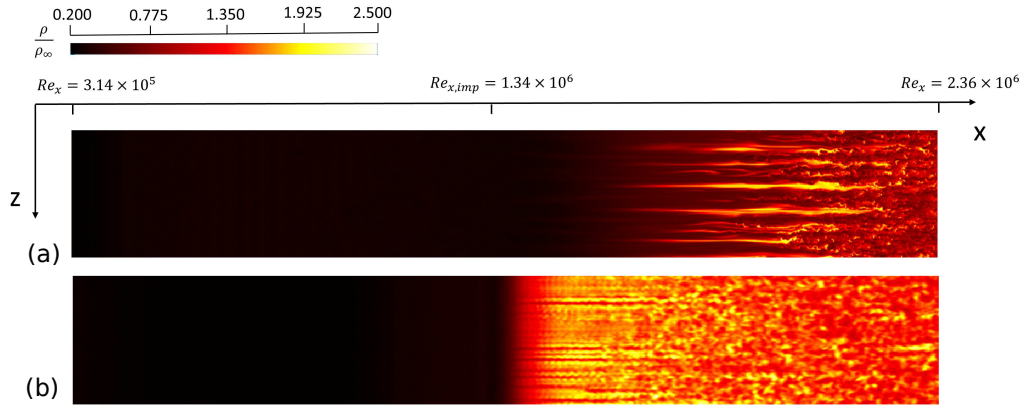


FIGURE 5. Instantaneous density contours for $\alpha = 7^\circ$ on a wall-parallel plane located at $y/\delta_o^* = 0.55$ in DNS (top) and WMLES (bottom).

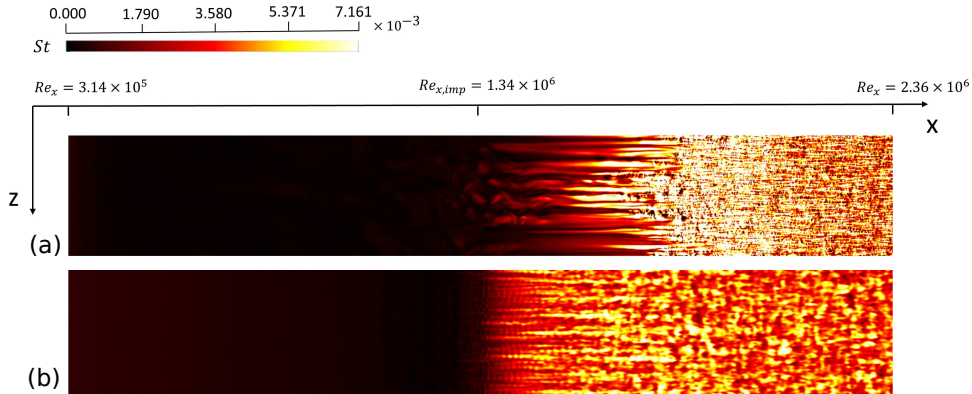


FIGURE 6. Instantaneous contours of the Stanton number for $\alpha = 7^\circ$ on the wall in DNS (top) and WMLES (bottom).

that ellipticity is provided through the boundary conditions at the matching location, or equivalently, unless a portion of the elliptic zone of the flow is resolved by the WMLES grid. The results indicate that these requirements may not be satisfactorily met in these

simulations, which calls for potential incorporation of non-equilibrium or slip wall models that could account for streamwise transport.

4. Conclusions

In this study, equilibrium WMLES has been compared against DNS for addressing the performance of the former in predicting shock-induced transition and heating in hypersonic boundary layers. In this flow, the equilibrium wall model underperforms in a number of different metrics. At low shock-incidence angles, the post-shock boundary layer in DNS is laminar, whereas it rapidly transitions to turbulence in WMLES. At higher incidence angles, both DNS and WMLES predict transition under no inflow disturbances, with WMLES results agreeing qualitatively with the overall trends in DNS. However, from a quantitative standpoint, WMLES underpredicts all of the following: (a) the size of the separation bubble by a factor of 2; (b) the post-shock peak skin friction by up to 30%; and (c) the post-shock peak aerodynamic heating rate by up to 30%. Overall, the considerations above suggest that upgraded wall models beyond the equilibrium one may be required to predict these phenomena.

These results, in conjunction with those reported in previous studies, suggest that the problem of predicting aerodynamic heating downstream of shocks impinging on transitional boundary layers with WMLES is remarkably challenging irrespective of the shock-incidence angle for the following reasons. On one hand, at low shock-incidence angles $\alpha \lesssim 6^\circ$, the disturbance made by the shock on the boundary layer is not sufficiently strong to trigger transition. As a result, inlet disturbances are required for the post-shock boundary layer to transition to turbulence by the synergistic action of the shock and the eigenmodes already growing upstream of the interaction zone. However, coarse grids of relevance for WMLES are not efficient at numerically supporting the propagation of inlet disturbances along the laminar portion of the boundary layer. Consequently, WMLES at low incidence angles requires either (a) a tuned increase of the amplitude of the inlet disturbances in order to compensate for their gradual numerical dissipation as they propagate downstream toward the shock, as done in Yang *et al.* (2017), or (b) the deployment of transition sensors to delineate the spatial region where the wall model should be turned on based on energy norms, as done in Mettu & Subbareddy (2018). However, none of those two alternatives, even if they were both purposely designed to match DNS results, would likely lead to any useful prediction when compared to results obtained from ground experiments, since the disturbances that prevail in hypersonic wind tunnels can be hardly characterized at present time to the level of detail required for their translation into fundamental modes that can be utilized in theoretical analyses or numerical simulations. The overall error made by DNS and WMLES predictions therefore cannot be presently isolated in this problem at low incidence angles, as clearly illustrated in Figure 13 in Yang *et al.* (2017), because shot-to-shot and facility-to-facility variations in data from ground experiments display large scatter, even if the experiments were all carried out with the same test model (Schülein 2014; Sandham *et al.* 2014; Willems *et al.* 2015). On the other hand, at higher shock-incidence angles $\alpha \gtrsim 6^\circ$, the boundary layer transitions to turbulence by the sole action of the shock wave. Although inlet disturbances become unnecessary for the completion of transition, which may facilitate the undertaking of numerical simulations and experiments, the present study shows several obstacles of different nature that hinder the performance of WMLES and arise as a consequence of complex aerothermodynamic effects. In particular, the intense spikes in

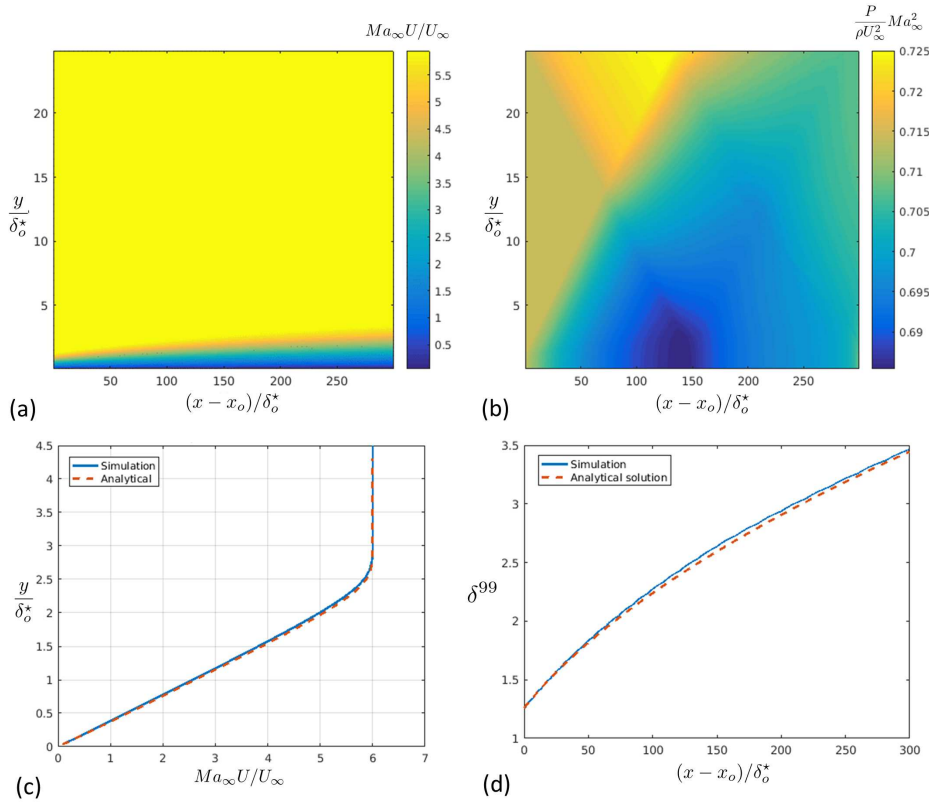


FIGURE 7. 2D numerical simulations of a Mach-6 hypersonic laminar boundary layer without incident shock: (a) Streamwise velocity contours and (b) static-pressure contours. The bottom panels include comparisons between 2D numerical simulations (solid lines) and similarity solutions (dashed lines) for (c) streamwise velocity profile evaluated at $(x - x_o)/\delta_o^* = 150$ and (d) streamwise evolution of the boundary-layer thickness.

skin friction and aerodynamic heating in the post-shock region, and the corresponding streaky flow structures that produce this thermomechanical augmentation, are not easily predicted by standard wall models. Similarly, the adverse pressure gradient generated by the incident shock wave leads to significant elliptic effects in the flow field, including long separation bubbles, that cannot be easily anticipated by equilibrium wall models.

Acknowledgments

This investigation was funded by the U.S. Air Force Office of Scientific Research (AFOSR) Grant #1194592-1-TAAHO. The authors are grateful to Dr. Jeffrey O'Brien and Dr. Frank Ham for useful technical discussions on this subject. Computational resources were provided by the U.S. Department of Energy.

Appendix: CharLES results for laminar hypersonic boundary layers

Comparisons between the similarity solution for the Mach-6 compressible boundary layer upstream of the shock, and results obtained using the present code in two-dimensional (2D) numerical simulations, are shown in Figure 7. The computational do-

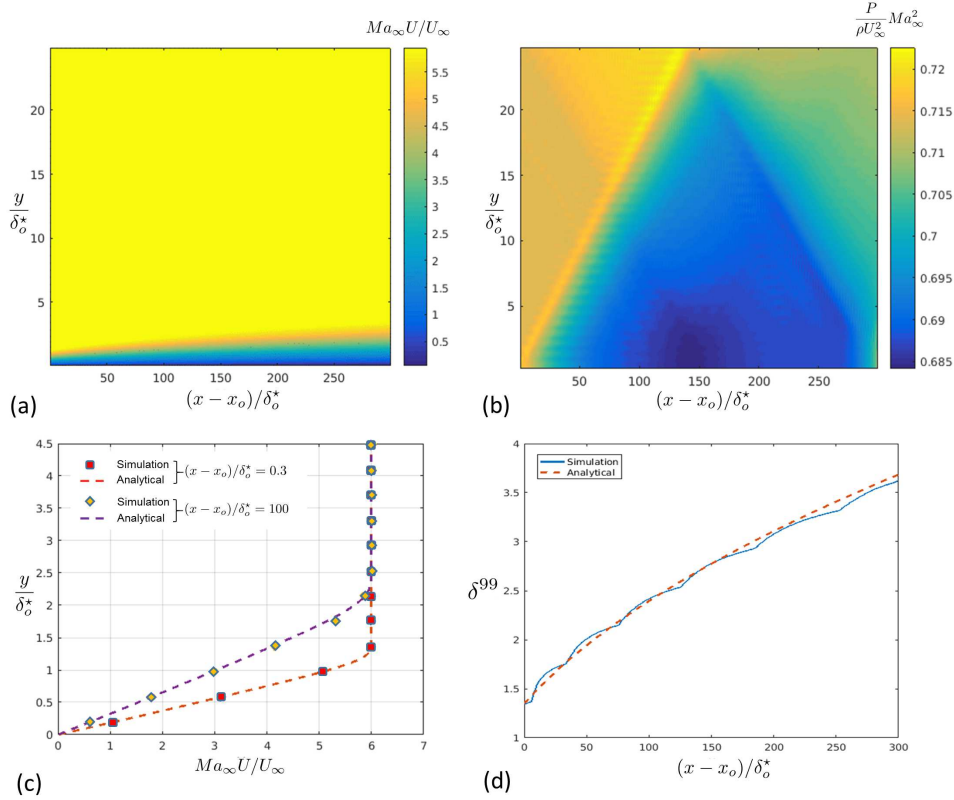


FIGURE 8. 2D numerical simulations of a Mach-6 hypersonic laminar boundary layer obtained using an equilibrium wall model without incident shock: (a) Streamwise velocity contours and (b) static-pressure contours. The bottom panels include comparisons between 2D WMLES (solid lines and symbols) and similarity solutions (dashed lines) for (c) streamwise velocity profile evaluated at two streamwise locations and (d) streamwise evolution of the boundary-layer thickness.

main is $300\delta_o^* \times 25\delta_o^*$ in the streamwise and wall-normal directions respectively, where δ_o^* is the inlet displacement thickness corresponding to $Re_{\delta_o^*} = 6830$. The grid resolution is 1500×150 cells. Note that the code reproduces reasonably well the similarity solution, as shown in panels (a), (c) and (d), despite an approximately 3% departure observed in panel (b) from the hypothesis of zero wall-normal pressure gradient that is necessary for the derivation of the similarity solution. The latter is an issue that is oftentimes overlooked in calculations at high Mach numbers, and which typically prevents numerical simulations from exactly matching the similarity solution even far from the leading edge.

Figure 8 shows similar comparisons as those in Figure 7 with the exception that the 2D numerical simulation results presented in Figure 8 are obtained by using the equilibrium wall model within the first cell near the wall. Specifically, the grid employed in Figure 8 has 512×64 cells. This amounts to 4 cells across the boundary layer very close to the inlet of the computational domain, as shown in Figure 8(c) for $(x-x_o)/\delta_o^* = 0.3$. Note that the equilibrium wall-model formulation is fundamentally different from the exact formulation of the laminar boundary layer, although both collapse to the same balances of stress and vorticity near the wall for zero pressure gradient, where the eddy viscosity in the wall model and the convective transport in the exact formulation become negligible.

REFERENCES

- BRÈS G., BOSE S. T., EMORY M., HAM F. E., SCHMIDT O. T., RIGAS G. AND COLONIUS T. 2018 Large-eddy simulations of co-annular turbulent jet using a Voronoi-based mesh generation framework. *AIAA Paper* 2018-3302.
- CANDLER, G. V. 2019 Rate effects in hypersonic flows. *Annu. Rev. Fluid Mech.* **51**, 379-402.
- HILDEBRAND, N., DWIVEDI, A., NICHOLS, J. W., JOVANOVIĆ, M. R. & CANDLER, G. V. 2018 Simulation and stability analysis of oblique shock-wave/boundary-layer interactions at Mach 5.92. *Phys. Rev. Fluids* **3**, 013906.
- KAWAI, S. & LARSSON, J. 2012 Wall-modeling in large eddy simulation: Length scales, grid resolution, and accuracy. *Phys. Fluids* **24**, 015105.
- LEYVA, I. A. 2017. The relentless pursuit of hypersonic flight. *Phys. Today* **70**, 30-36.
- METTU, B. R. & SUBBAREDDY, P. K. 2018 Wall modeled LES of compressible flows at non-equilibrium conditions. *AIAA Paper* 2018-3405.
- SANDHAM, N., SCHÜLEIN, E., WAGNER, A., WILLEMS, S. & STEELANT, J. 2014 Transitional shock-wave/boundary-layer interactions in hypersonic flow. *J. Fluid Mech.* **752**, 349–382.
- SCHÜLEIN, E. 2014 Effects of laminar-turbulent transition on the shock-wave/boundary-layer interaction. *AIAA Paper* 2014-3332.
- URZAY, J. 2018 Supersonic combustion in air-breathing propulsion systems for hypersonic flight. *Annu. Rev. Fluid Mech.* **50**, 593-627.
- VREMAN, A. 2004 An eddy-viscosity subgrid-scale model for turbulent shear flow: Algebraic theory and applications. *Phys. Fluids* **16**, 3670–3681.
- WILLEMS, S., GÜLHAN, A. & STEELANT, J. 2015 Experiments on the effect of laminar-turbulent transition on the SWBLI in H2K at Mach 6. *Exp. Fluids* **56**, 49–68.
- YANG, X. I. A., URZAY, J., BOSE, S. T. & MOIN, P. 2017 Aerodynamic heating in wall-modeled large-eddy simulation of high-speed flows. *AIAA J.* **56**, 731–742.